A crawling robot driven by multi-stable origami

IOP Publishing Smart Materials and Structures
Smart Mater. Struct. 26 (2017) 094007 (11pp) https://doi.org/10.1088/1361-665X/aa721e

A crawling robot driven by multi-stable origami

Alexander Pagano, Tongxi Yan, Brian Chien, A Wissa and S Tawfick[1]

University of Illinois Urbana-Champaign, Urbana, IL, United States of America

E-mail: tawfick@illinois.edu

Received 27 January 2017, revised 18 April 2017
Accepted for publication 10 May 2017
Published 17 August 2017

Abstract

Using origami folding to construct and actuate mechanisms and machines offers attractive opportunities from small, scalable, and cheap robots to deployable adaptive structures. This paper presents the design of a bio-inspired origami crawling robot constructed by folding sheets of paper. The origami building block structure is based on the Kresling crease pattern (CP), a chiral tower with a polygonal base, which expands and contracts through coupled longitudinal and rotational motion similar to a screw. We design the origami to have multi-stable structural equilibria which can be tuned by changing the folding CP. Kinematic analysis of these structures based on rigid-plates and hinges at fold lines precludes the shape transformation associated with the bistability of the physical models. To capture the kinematics of the bi-stable origami, the panels' deformation behavior is modeled utilizing principles of virtual folds. Virtual folds approximate material bending by hinged, rigid panels, which facilitates the development of a kinematic solution via rigid-plate rotation analysis. As such, the kinetics and stability of folded structures are investigated by assigning suitable torsional spring constants to the fold lines. The results presented demonstrate the effect of fold-pattern geometries on the snapping behavior of the bi-stable origami structure based on the Kresling pattern. The crawling robot is presented as a case study for the use of this origami structure to mimic crawling locomotion. The robot is comprised of two origami towers nested inside a paper bellow, and connected by 3D printed end plates. DC motors are used to actuate the expansion and contraction of the internal origami structures to achieve forward locomotion and steering. Beyond locomotion, this simple design can find applications in manipulators, booms, and active structures.

Supplementary material for this article is available online

Keywords: origami, bistability, active structures

(Some figures may appear in colour only in the online journal)

1. Introduction

We seek inspiration from natural systems which overcome an incredible variety of challenges with simple, adaptive solutions to make deployable and reconfigurable systems more adaptive, less obtrusive, and more independent. Many diverse systems in nature depend on the controlled actuation of flexible structures through buckling instabilities for rapid motion in both predation and locomotion [1–3]. For example, rapid motion of plants demonstrates how categorically slow moving systems have adaptively developed mechanisms that allow for fast motion [4]. The snap-buckling closure of Venus flytraps is due to the reconfiguration from convex to concave curvature of its leaves, driven by a change in turgor pressure. Due to geometric constraints, this curvature is coupled with a stretching deformation mode that stores elastic energy which allows small perturbations in curvature to result in large, rapid motion [1]. A similar mechanism is used in the beaks of hummingbirds to produce a fast-closing action at speeds unattainable by direct muscular control. The pre-configuration of an anisotropically compliant bone in the hummingbird beak allows for smooth flexion to a strained position which is triggered to facilitate the fast expenditure of elastic energy as the beak snaps back to its closed equilibrium state [3]. Buckling instability has also been shown to

[1] Author to whom any correspondence should be addressed.

be a dominant feature of locomotion for uni-flagellated bacteria, suggesting that the bi-stable actuation scheme is viable independent of scale [2]. In this paper, we utilize origami as a platform for the scale-free investigation of actuation based on the buckling instabilities of thin, flexible features.

The outstanding number of natural creatures that utilize folding highlights the potential of origami for a variety of applications at different length scales. The investigation of natural folding yields a wealth of useful folding schemes, among which are the ubiquitous Miura-ori pattern [5] and the Kresling pattern [6] which is investigated here. These structures have broad-reaching applications in deployable, rigidizable, and multi-functional systems. Through the manipulation of 'defect states' created by the buckling of thin sheets, origami also provides the framework for the development of reprogrammable, mechanical metamaterials [7]. Simplistic tools for the modeling of these structures such as rigid-panel analysis and the principles of virtual folds enable facile investigation of their properties so that the development of useful structures is straightforward [8].

The ability to produce a functional and geometrically complex 3D mechanical system from a flat sheet introduces exciting opportunities in the field of robotics for remote, autonomously deployable systems or low cost integrated locomotion. Self-folding origami robots have demonstrated the viability of folded monolithic structures for a variety of tasks [9–11]. For example, Rus, Wood and co-workers demonstrated how self-assembly can be used to create a deployable robot that folds itself from a flat sheet and walks away [10] and the diversity of origami patterns which are useful for locomotion [9]. The reconfigurable nature of origami systems often allows for a multitude of potential functional folding schemes within a given structure. Moreover, in a monolithic system where load-bearing structure and locomotion are facilitated by the same components, this reconfigurability lends itself to multi-model and multi-functional design. For example, the Tribot 'robogami' is capable of moving via both jumping and crawling locomotion by the same actuation mechanism [12] which provides more opportunities for success when navigating unpredictable terrains. Multi-functional design facilitated by folded structures has the potential to simplify robotics design through the integrated use of coupled structural and actuation mechanisms while decreasing both weight and fabrication costs.

A number of researchers have investigated the origami structure discussed in this manuscript. Relevant contributions and methods are discussed in the following literature review: Kresling [6] presents the 'Kresling pattern' as the natural result of twisting a paper cylinder until it buckles. This twist-buckling causes the formation of curved fold lines which align well with the crease pattern (CP) which takes its name from this discovery. The folded geometry is investigated, but folding behavior is not discussed. Wilson *et al* [13] presents an application for the Kresling pattern as a deployable sunshade for telescopes. In this work, the folding behavior is investigated using a simple wireframe model where fold lines are represented by rigid bars and kinematically necessary deformation is determined from a simple strained link model as used in section 3. Cai *et al* [14] investigated the rigid foldability of the Kresling pattern using the quaternion rotation sequence method and determined that the structure is not rigidly foldable between open and closed configurations. Cai *et al* [15] also study the folding behavior of a stack of building blocks as presented herein. In this work, a wireframe model is used which approximates fold lines as bars and determines the associated strains and nodal loads during the folding evolution, similar to section 3. Each building block is considered separately, and the buckling modes of the tower are discussed.

In this study we demonstrate the design, analysis and fabrication of a bi-stable origami structure inspired by the Kresling pattern. Through the coupling of rotational and linear motion, this structure uses buckling instabilities to accomplish large-stroke snapping motion from relatively small inputs. We demonstrate the functional application of this mechanism in the case study with a crawling robot that utilizes monolithic, multi-functional design to realize locomotion from a single motor. The work presented in this manuscript expands on the existing literature by investigating kinematically necessary deformation in a physically realizable mode (bending). The use of virtual fold lines allows for a simple representation of bending using discretized segments as in the rod and pin approach. Cuts are added to the pattern to enable the folding of extreme tower geometries which are not considered in the existing literature, therefore stronger bistability is attained with the pattern including cuts. Finally, the origami structure is proposed as an actuation mechanism rather than a structural element alone, demonstrating the validity of this structure for monolithic design. The remainder of this paper is organized as follows: section 2 presents the design and mechanics of the origami structures; sections 3 and 4 detail the kinematics of the origami structure represented as rigid panels; section 5 presents the crawling robot design and experimental results as a case study.

2. Design and mechanics of the origami

2.1. Geometric description of the origami structure

The origami structure can be uniquely defined by the three parameters, n, R, and λ, which are the number of sides of the basal polygon, the circumradius of the basal polygon, and the helical angle ratio, respectively [16]. The angle ratio, λ, is the ratio of the angle of the diagonal crease $\overline{AB}$ (figure 1(B)) to half the internal angle of the basal polygon. This helical angle ratio determines the aspect ratio of the structure and the degree of transformation during folding. It is bounded by $0.5 \leqslant \lambda \leqslant 1.0$ where $\lambda = 0.5$ represents an origami height $H = 0$ with indistinguishable open and closed states, constructed from two offset polygonal bases connected by triangular panels. The upper bound where $\lambda = 1.0$ is a special case where creases b and a are perpendicular. If and only if $\lambda = 1.0$, the final height is given by $H = b = l\sin(\lambda\theta)$ due to the diagonal crease angle being equal to 180° (see figure 1 where $\lambda = 0.8$, and $H \neq b$). $\lambda > 1.0$ simply indicates a change in handedness/chirality, defined here as the direction of rotation, α, which results in expansion of the structure. From these parameters, the remaining fold lengths and angles

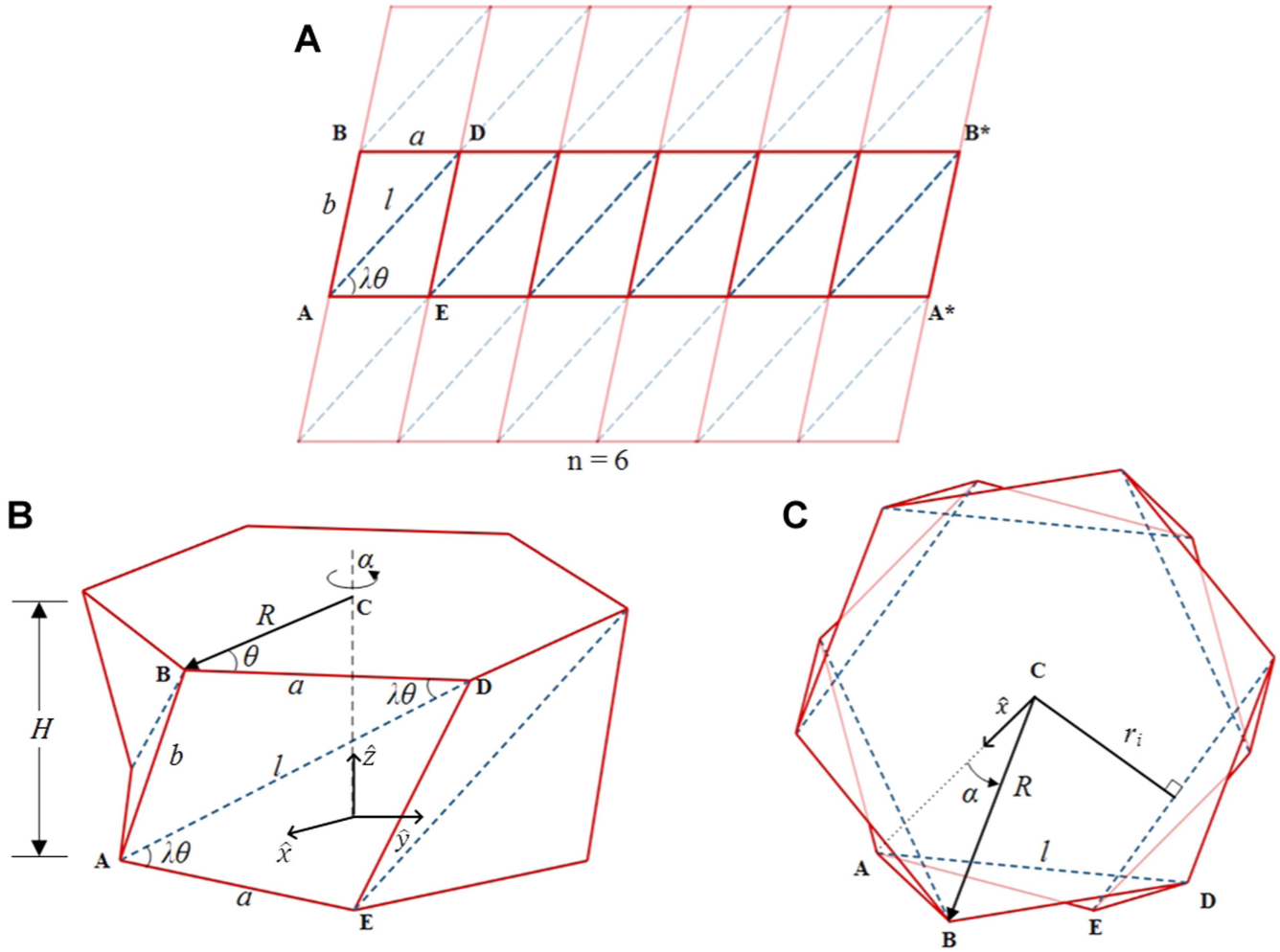

Figure 1. Geometry of the origami structure. (A) The crease pattern (CP) for the polygonal prism origami structure shown in (B) which is derived from the Kresling Pattern [6]. Mountain folds are shown as solid, red lines and valley folds are shown in dashed blue. The schematics define the geometric parameters: n is the number of sides, a is the *p*olygon side length, l is the diagonal valley-crease length, b is the side panel length, the angle θ is half the internal angle of the basal polygon, and λ, the angle ratio, is a metric of transformation between open and closed states and can vary between 0.5 and 1. (B) A hexagonal-based Kresling origami is constructed from the shaded pattern in (A) where $n = 6$ and $\lambda = 0.8$. Variation in circumradius R results in scaling the size of this origami. Also shown is rotation angle, α, for rotation of the top polygon about the dashed axis shown in (B). (C) Top down view of the structure shown in (B) while in its closed position. The crease length of the diagonal valley-fold, l, is determined trigonometrically from this schematic. The internal radius, r_i, of the cavity formed by the valley-folds while in the closed position is also determined from this view. The rotation angle, α, is measured from the $\hat{x}$-axis to the vector $\boldsymbol{R}$ as shown. The $\hat{x}$-axis is chosen to intersect the first vertex of the bottom polygon, labeled (A). The $\hat{z}$-axis points upwards along the axis of rotation labeled α in (B), and the $\hat{y}$-axis follows the right hand rule convention.

are easily determined geometrically from the generic CP (figure 1(A)) and basic polygon relations. The governing equations used to create the CP for a specific structure are given in equations (1)–(3), developed from [16].

The construction of the structure from the flat CP (figure 1(A)) is accomplished by folding and rolling it into polygonal prism such that points A and B overlap with A* and B*, which results in the expanded or 'open' structure (figure 1(B)). When a force is applied on the top of the structure (while allowing free rotation), it twists and contracts while exhibiting a snapping motion from the open to closed positions as demonstrated in figure 2. This transformation is non-rigid in that, in addition to the local folding of the mountain and valley crease lines, elastic deformation of the flat panels is required to complete the transformation. For simplicity in discussion we will refer to the transition from open to closed positions as '*contraction*' and the inverse transformation from closed to open '*expansion*'. Depending on the value of λ, when the origami is fully folded, an internal cavity is formed with some internal radius, r_i. This internal radius is characteristic of the polygon formed by the valley folds when in the closed position, and is determined trigonometrically from the same closed configuration used to determine the crease length, l (equation (5), see figure 1(C)). The geometric relations derived from figure 1(C) are listed in equations (4), (5).

$$a = 2R \sin\left(\frac{\pi}{n}\right), \tag{1}$$

$$b = (l^2 + a^2 - 2la\cos(\lambda\theta))^{1/2}, \tag{2}$$

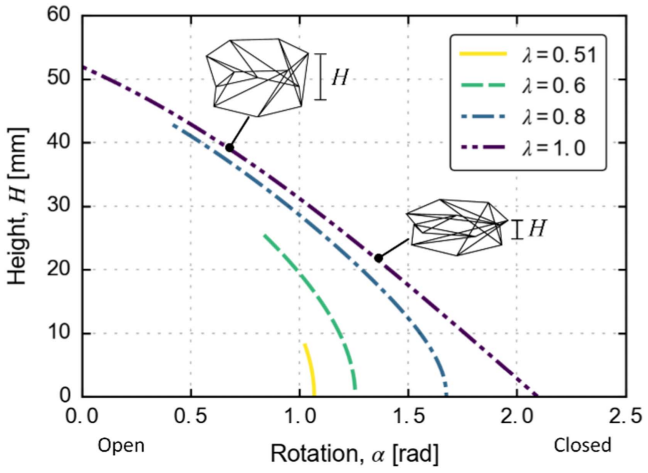

Figure 2. Change in origami height, H, calculated as a function of rotation angle, α, to demonstrate contraction of the origami. Height is plotted for values of angle ratio, λ, spanning its range of $0.5 < \lambda \leqslant 1.0$ to demonstrate the effect of λ on the extent of transformation during contraction. Note that as λ approaches 0.5, origami height and rotation vary less between initial (open) and final (closed) states than for larger values of λ.

$$\theta = \frac{\pi(n-2)}{2n}, \tag{3}$$

$$l = 2R\cos(\theta(1-\lambda)), \tag{4}$$

$$r_i = R\sin(\theta(1-\lambda)). \tag{5}$$

When the origami is constructed from the CP into the open position (figure 1(B)), its configuration is expressed by its height, H, and the rotation angle, α, which describes the rotation of the top polygon with respect to a frame fixed to the bottom polygon. The chirality of the structure can be changed by taking the mirror image of the CP in figure 1(A) reflected about a vertical axis. The origami structure shown in figure 1(B) has negative chirality but positive and negative chirality are mathematically indistinguishable when considering the behavior of the structure during expansion or contraction.

2.2. Foldability analysis for rigid origami

The CP for a single origami building block shown in figure 1(A) is comprised of one row of n parallelogram panels. This CP is rigid foldable, which indicates that the polygonal prism can be constructed from a flat CP by simply bending the fold lines without deforming the flat panels. This rigid foldability can be confirmed by analyzing the number of degrees of freedom (DOF) for the vertices,

$$\mathrm{DOF} = N - 3, \tag{6}$$

where N is the number of mountain or valley folds that meet at a vertex [17]. In this system, each vertex has the same $N = 4 - 3 = 1$ and for each unit cell, there will be n vertices in series and therefore $\mathrm{DOF_{CP}} = n(N-3)$ and the folding of a sheet from a flat state to the polygonal prism in the open configuration is possible by rigid folding. However, folding from the open to closed configuration is not possible by rigid folding as will be discussed in the following sections [17]. Following the creasing of mountain and valley folds, the vertices corresponding to the 1st and nth panel (for example A, B and A*, B* in figure 1(A)) are overlapped to create the basal polygon. Notably, for $\lambda > 0.5$, the overlap can be done in such a way to construct a bi-stable structure with distinct open and closed shapes (inset figure 2). Once the vertices are fixed to one another (e.g. by gluing), the formed origami structure is kinematically rigid in both of these configurations. This additional constraint, created by gluing the vertices, fully defines the position of each vertex with respect to its neighbor so that the structure no longer has available DOF. In other words, if the panels are truly rigid, the expanded polygonal prism having $\lambda > 0.5$ cannot be transformed between states. If the panels are bendable, the polygonal prism exhibits snapping between the expanded and contracted configurations. However, it is not readily apparent from the CP what the physical shape, as represented by the values of height, H, and rotation angle, α, is at these stable positions.

3. Kinematic analysis of rigid panels and folding joints

To determine the configuration of the folded origami structure, a vector loop equation for the closed loop, $\boldsymbol{R_{BA}}$, $\boldsymbol{R_{BC}}$, $\boldsymbol{R_{DC}}$, $\boldsymbol{R_{DA}}$, was solved numerically using a custom Python program.

$$\boldsymbol{R_{BA}} - \boldsymbol{R_{BC}} + \boldsymbol{R_{DC}} - \boldsymbol{R_{DA}} = \boldsymbol{0}, \tag{7}$$

$$\boldsymbol{R_{BA}} = R(-1 + \cos\alpha)\hat{x} + R\sin\alpha\,\hat{y} + H\,\hat{z}, \tag{8}$$

$$\boldsymbol{R_{BC}} = R\cos\alpha\,\hat{x} + R\sin\alpha\,\hat{y} + 0\,\hat{z}, \tag{9}$$

$$\boldsymbol{R_{DC}} = R\cos\left(\alpha + \frac{2\pi}{n}\right)\hat{x} + R\sin\left(\alpha + \frac{2\pi}{n}\right)\hat{y} + 0\,\hat{z}, \tag{10}$$

$$\boldsymbol{R_{DA}} = R\left(-1 + \cos\left(\alpha + \frac{2\pi}{n}\right)\right)\hat{x} + R\sin\left(\alpha + \frac{2\pi}{n}\right)\hat{y} + H\,\hat{z}. \tag{11}$$

The following constraints were used to attain the numerical solution for height and rotation in the initial position, i.e. open:

(1) The angle between vectors $\boldsymbol{R_{BD}}$ and $\boldsymbol{R_{DA}}$ is $\lambda\theta$

$$\boldsymbol{R_{BD}} \cdot \boldsymbol{R_{DA}} = -(la)\cos(\lambda\theta). \tag{12}$$

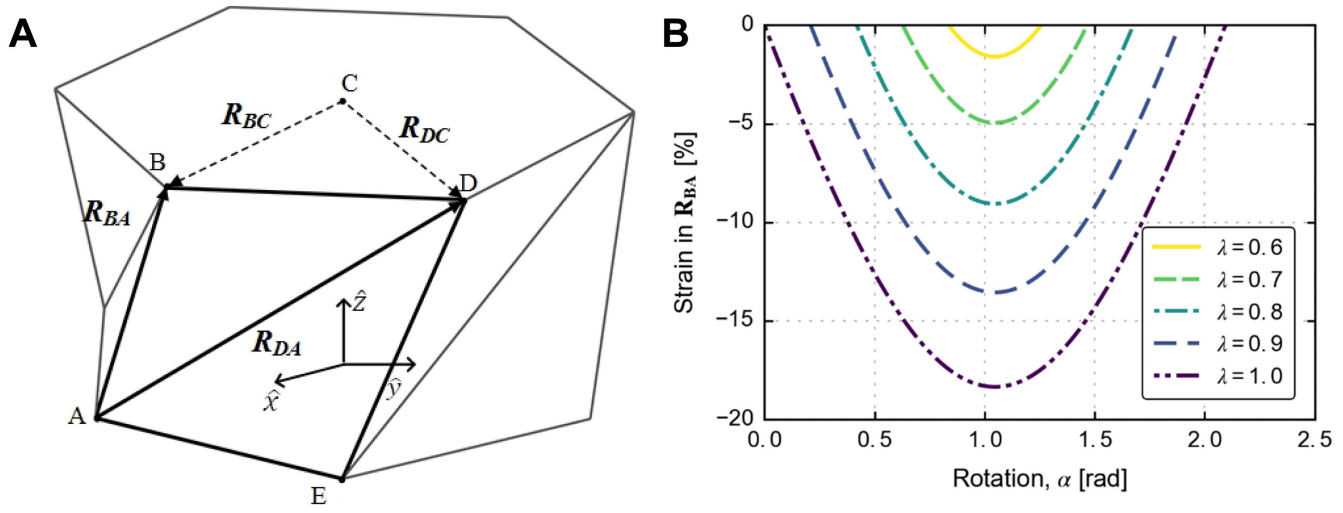

Figure 3. (A) The origami structure shown in the open position, where the vertices and representative vectors used in the vector loop equation are shown. The thick black lines represent the *n*th panel, of which the triangular 'unit cell' $\overline{ABD}$ is sufficient to determine the motion of the structure during contraction or expansion. All other positions can be determined through arbitrary rotations. The structure shown represents $R = 30$ mm, $\lambda = 0.8$ and $n = 6$. (B) Theoretical strain in vector $\boldsymbol{R_{BA}}$ as a function of rotation is plotted here for several values of angle ratio, λ, to demonstrate the effect of λ on the bi-stable behavior of the tower. Theoretical strain is given here as a metric for the extent of deformation required for expansion or contraction of the structure between kinematically allowable open and closed positions. As the angle ratio, λ, increases, the theoretical strain increases so that more deformation is required for higher values of angle ratio.

(2) The fold $\overline{AD}$ is a rigid line represented by a vector $\boldsymbol{R_{DA}}$ with magnitude l

$$\|\boldsymbol{R_{DA}}\| = l. \tag{13}$$

Using the Newton–Raphson method, the constraint equations are numerically solved by systemically varying the components of the vector loop vectors until the correct solution was found. In this way, the initial rotation angle was determined by solving the first constraint, which was then used in conjunction with the second constraint to determine the structure's initial height. Once the open configuration was defined, the final rotation was determined geometrically from the closed position where $H = 0$ by definition. As previously stated, folding from the open to closed position requires some non-rigid deformation of the CP. To investigate the behavior of the structure during expansion and contraction we mathematically allowed the length of vector $\boldsymbol{R_{BA}}$ (equivalent to $\boldsymbol{R_{DE}}$) to vary throughout folding. This introduces an additional degree of freedom that allows the model to smoothly transition from open to closed positions, thus conceptually simplifying the expression of deformation to a single dimension. Therefore, the kinematically necessary deformation can be quantified by simple strain as a function of tower parameters such as λ. Contraction was then simulated by stepping from initial to final rotation angles with equal step size. Height was then determined at each rotational step to fully define the configuration of the structure during expansion or contraction. The parameter of 'rotation' was specifically chosen as the input here since it is a relevant input for the motor-driven locomotion of the case study.

The degree of deformation required for folding, which, as discussed later, is a direct measure of the bistability of the system, can then be quantified by calculating the theoretical change in free length R_{BA} (figure 3). However, this simple strain is not representative of the observed deformation. Our physical paper models realize the additional degree of freedom through the use of relief cuts along folds $\overline{AB}$. These cuts allow the length of $\boldsymbol{R_{BA}}$ to vary through the bending of adjacent panels so that corners A and B contract in the z-direction. This bending describes the motion of physical models better than simply strained links—as the primary deformation mode of paper is bending not stretch—and can be modeled as the bending of the triangular panels $\overline{ABD}$ and $\overline{AED}$ on either side of the diagonal valley-fold $\overline{AD}$.

4. Kinematic analysis including virtual folds

To account for panel bending, a 'virtual fold' can be mathematically created between 2 vertices across a bending panel [8, 18]. Virtual fold assumes that mathematical fold lines can be added to represent the 'hidden' DOF associated with the out of plane bending modes in kinematically rigid panels. To capture the bending behavior observed experimentally, virtual folds are placed along $\boldsymbol{R_{FD}}$ and $\boldsymbol{R_{F'A}}$ for each panel as shown in figure 4. In this way, each panel was divided into triangular facets $\overline{AFD}$, $\overline{BFD}$, $\overline{AF'D}$, and $\overline{AF'E}$ whose surface normals are parallel when panels are unbent (i.e. open and closed configurations, figure 2) and have a non-zero scalar product during bending (figure 5). Triangular facets $\overline{AF'D}$ and $\overline{AF'E}$ can be represented as rotations of facets $\overline{AFD}$ and $\overline{BFD}$ and are therefore mathematically redundant. To simplify this discussion we will only consider the bending of virtual fold $\overline{FD}$.

The position of the virtual fold was chosen to emulate the conditions observed in physical models, but could be given any arbitrary position. At each step during contraction, the vertex of the virtual fold line which lies at point D on the top

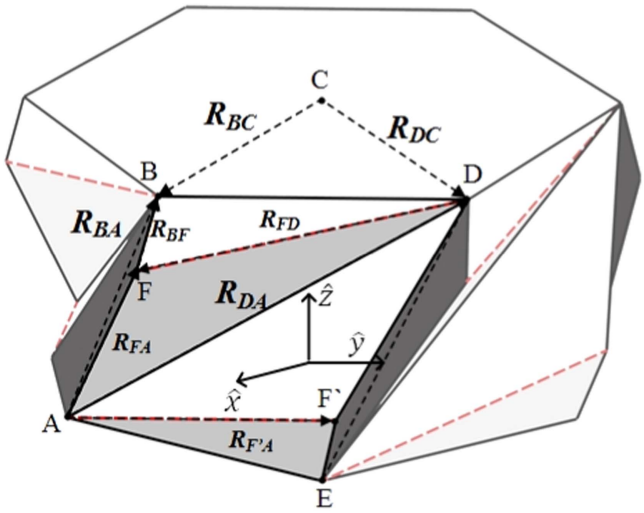

Figure 4. Accounting for panel bending by introducing virtual folds. During contraction, deformation is facilitated by out-of-plane bending of the triangular panels $\overline{ABD}$ and $\overline{AED}$. The bending of these panels is treated rigidly through the introduction of virtual folding lines along $\overline{FD}$ and $\overline{AF'}$. The folding angle (e.g. θ_{BD}) is the dihedral angle between panels intersecting at fold line (e.g. $\overline{BD}$). Angles not shown for readability in print.

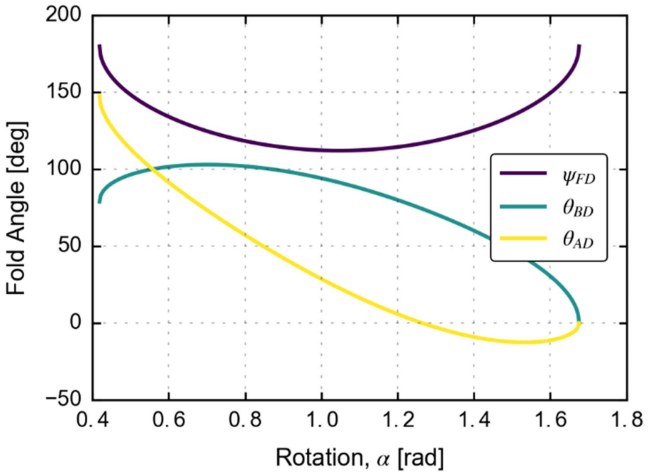

Figure 5. Characteristic fold angles as a function of rotation, determined from the scalar product of their respective surface normal vectors. Fold angles can be considered the angle between the facets on either side of the fold line. The fold angle, ψ_{FD}, corresponds to virtual fold lines $\overline{FD}$ and $\overline{AF'}$. The virtual fold angle is initially and terminally 180 degrees due to the unbent structure in the open and closed configurations. The fold angles θ_{BD} and θ_{AD} of creases $\overline{BD}$ (same as $\overline{AE}$) and $\overline{AD}$ take their initial values due to the geometric constraints of the structure in the open configuration. The negative angles are caused by the intersection of virtual facets.

polygon remains fixed, while vertex at F is free to move according to the following constraints:

(1) The sides of the virtual facets must sum to the crease length, b, as defined in the CP (figure 1(A)) and equation (2). Each side has fixed length according to the rigid-panel assumption.

$$\|\boldsymbol{R_{FA}} + \boldsymbol{R_{BF}}\| = b. \tag{14}$$

(2) The virtual fold length, $\|\boldsymbol{R_{FD}}\|$, is fixed throughout contraction. This fold length, l_d, is determined from the open configuration (figure 3(A))

$$\|\boldsymbol{R_{FD}}\| = l_d. \tag{15}$$

(3) The extent of out of plane deflection is determined trigonometrically from triangle $\overline{ABF}$ where the change in length R_{BA} is given by the strain (figure 3(B)) while the lengths of $\boldsymbol{R_{BF}}$ and $\boldsymbol{R_{FA}}$ are fixed.

These constraint equations were numerically solved using the Newton–Raphson method as before. This allows for the position of each vertex to be determined at every step of expansion or contraction. From this, the fold angles can be determined by the scalar product of the surface normals of each facet (figure 5).

For the nth panel of an n-sided polygonal prism represented as $\overline{ABDE}$ we need only consider the fold angles of the folds, $\overline{BD}$, $\overline{FD}$ and $\overline{AD}$ to characterize the entire structure since all other folds are rotationally symmetric. To analyze the potential energy associated with the origami snapping motion, torsional springs can be attached to the virtual fold lines to calculate the restoring force resulting from the bending of each triangular panel. This kinetic treatment is used to investigate the bistability of the structure.

4.1. Analysis of the origami bistability

By treating fold lines as torsional springs where the crease lines given by the CP have a different spring constant than the virtual folds which approximate panel bending, all of the material properties can be condensed into a single non-dimensional parameter, namely the fold stiffness ratio, k_b/k_c, which is the ratio of torsional spring constants associated with virtual folds and creases (k_b and k_c respectively). These spring constants can be experimentally measured. For the results presented here, the torsional spring constants determined experimentally by Silverberg *et al* for 120 lb paper were used. These value were $k_c = 170 \pm 20$ mN m rad^{-1} for creases and $k_b = 6$ N m rad^{-1} for virtual folds [8].

The development of elastic energy during expansion or contraction as determined through the use of virtual folds and appropriate torsional springs can then be used to study the bistability of folded origami structures. The fold energy is given by the product of torsional spring potential and the length of the fold. For each fold, the associated folding energy is calculated and summed according to equation (16).

$$U_{\text{total}} = \frac{k_c}{2}\sum_{i=1}^{n}[2a(\theta_{BD,i} - \theta_{BD,0})^2 + l(\theta_{AD,i} - \theta_{AD,0})^2] + \frac{k_b}{2}\sum_{i=1}^{n}2l_d\psi_{FD,i}{}^2. \tag{16}$$

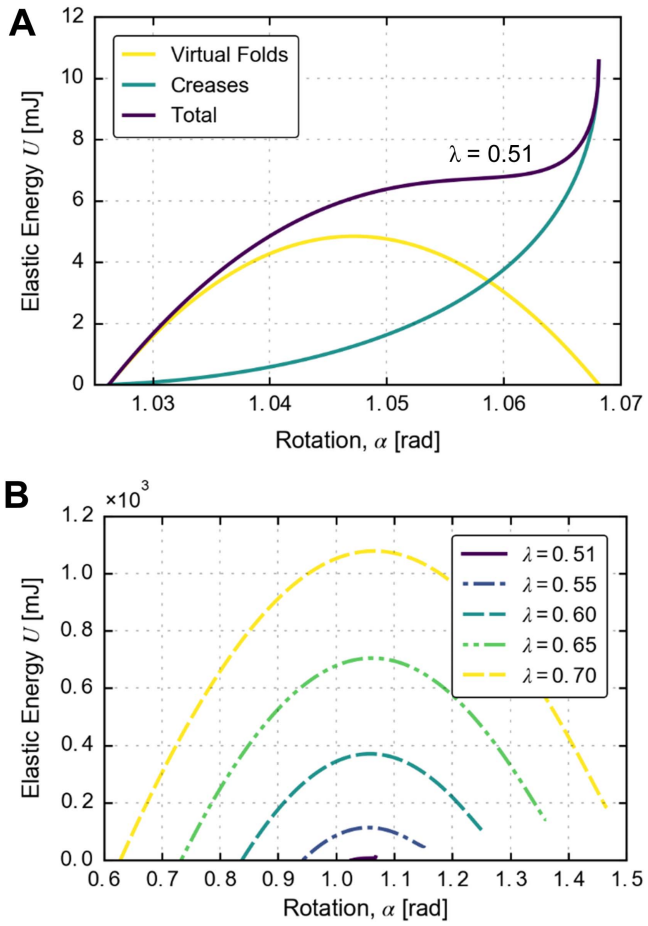

Figure 6. (A) Elastic energy contributions from creased folds and virtual folds are plotted as a function of rotation angle. The total elastic energy as determined by equation (16), is shown for λ equal to 0.51, and the ratio of k_b/k_c leads to an origami structure stable only in the expanded state. Here rotation angle increase corresponds to contraction of the origami, and creased lines have folding energies that are zero when in the open configuration. (B) The total elastic energy from equation (16) is plotted as a function of rotation for various λ to demonstrate that the potential energy barrier associated with bistability is more pronounced for larger angle ratios.

The equilibrium position for the torsional spring potential is assumed to be the open configuration, and is represented by the subscript $_0$. The total elastic energy of the origami structure is determined from equation (16) and plotted as a function of rotation in figure 6 to investigate the bistability of the structure during expansion and contraction.

Each $1/2kx^2$ term of equation (16) represents the energy contribution from a single fold. The contributions from each fold are summed first for each of n sides, then the energy of folding each side is summed to attain the energy to fold the entire structure. The scalar multiplier in front of each squared term can be used as a reference to the fold that is represented by that term. For example, $\frac{k_c}{2}2a(\theta_{BD,i} - \theta_{BD,0})^2$ gives the elastic energy of both folds (due to the multiplier of 2) with length a. As the structure has axial symmetry, $\theta_{XX,i}$ and $\psi_{XX,i}$ will be the same for $i = 1, 2, 3\ldots n$. Changing the fold stiffness ratio, k_b/k_c, scales the contributions from virtual folds and creases. It is the relative contribution of these terms which determines the stability of the open configuration, and therefore the strength of snap-through bistability (figure 6(A)). The results from equation (16) are shown in figure 6. The origami structures have a maximum potential energy at a certain rotation angle which corresponds to the snapping motion. The bistability is more pronounced for higher aspect ratio polygonal prisms (defined by larger λ values). Importantly, since the deformations that occur are elastic, the system is able to repeatedly move from one kinematical configuration to another through bi-stable snapping motion. In physical models, the thickness of folded layers prevents the system from accessing its co-planar, closed configuration. Instead, a force balance is established resulting in an equilibrium position at some nonzero height that can be conceptually correlated to the closed configuration of the structure. For the structure to be bi-stable, the elastic energy of the open and closed equilibrium configurations must be minimum energy states of the transformation. The energy required to produce the kinematically necessary deformations (i.e. panel bending) is then the barrier energy that separates the two equilibrium positions. It can be seen from figure 6(A) that bi-stable behavior begins to occur at low values of λ near its minimum of 0.5. However as λ increases to its maximum, more deformation is required and therefore the behavior is increasingly bi-stable. The onset of bistability is a function of the fold stiffness ratio and the origami structure parameters n, R, and λ. Since the material properties dictate the fold stiffness ratio and we are free to specify the structure parameters to fit our purposes, this structure serves as a tunable bi-stable system created from a flat sheet.

The energy as a function of rotation can then be used to determine the torque associated with holding the structure in a certain configuration. This was accomplished using the force energy relation in equation (17). The work required for each rotational step is then given by equation (18). This can then be related to the rotational and linear stiffness of the structure by equations (19) and (20).

$$\tau = -\frac{\partial U}{\partial \alpha}, \tag{17}$$

$$W = \tau \Delta\alpha, \tag{18}$$

$$K_{\text{rotational}} = \frac{2W}{(\Delta\alpha)^2}, \tag{19}$$

$$K_{\text{linear}} = \frac{2W}{(\Delta H)^2}. \tag{20}$$

The rotational and linear stiffness of the structure during contraction are shown in figure 7. Regions of negative stiffness demonstrate the bistability of the structure, where a small perturbation carries the structure through a large displacement.

In summary, this origami pattern, based on the Kresling pattern, demonstrates bi-stable expansion and contraction facilitated by the buckling of thin panels. This structure can be uniquely specified by the three parameters n, R and λ which are respectively the number of sides of the basal polygon, the circumradius of the basal polygon and the angle ratio. Through these parameters and the selection of the fold

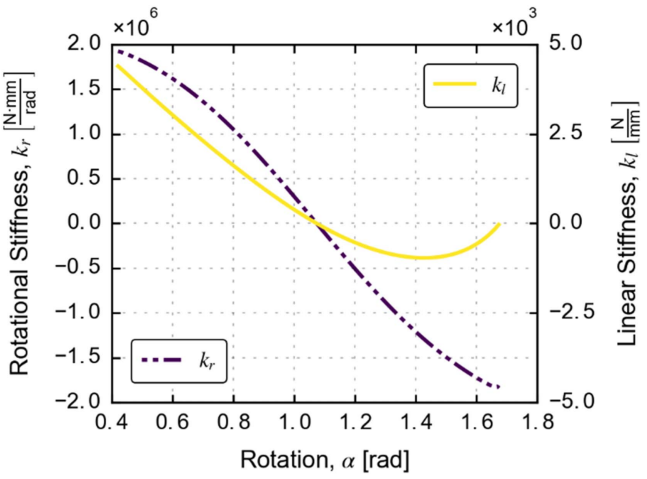

Figure 7. Rotational and linear stiffness as determined by equations (19) and (20) plotted as a function of rotation. The dashed line shows rotational stiffness and is plotted on the left axis (scaled by 10^6) while the solid line shows linear stiffness and is plotted on the right axis (scaled by 10^3). The upwards hook in linear stiffness is caused by the residual restoring force in the creased fold-lines.

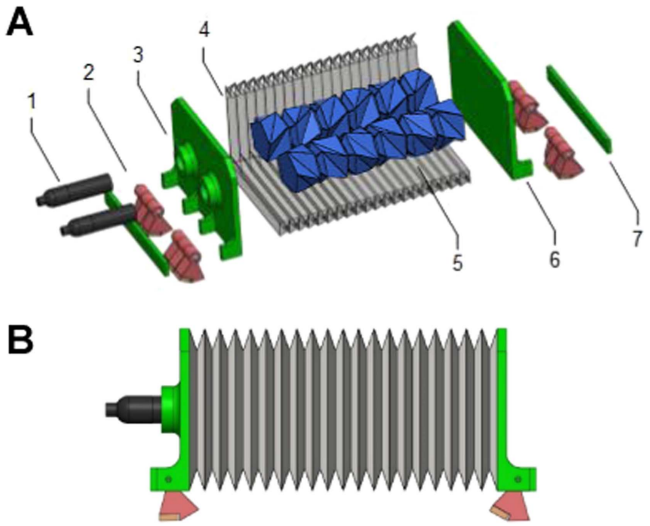

Figure 8. (A) Exploded view of CAD model. (1) Motors (2) Feet (3) Rear faceplate (4) Origami bellow (cutaway for visibility) (5) Origami towers (6) Front faceplate, torque-limiting coupling not shown (7) Stop limits foot rotation. (B) CAD model side view, colored for clarity. Photos shown in figure 9(C)/(D). Faceplates produced with Viper SI SLA machine using Somos® WaterClear resin.

stiffness ratio by material choice, the folding behavior of the structure can be fully determined and exploited. As a demonstrative example of the applications of this structure, we present a case study wherein this origami pattern is used for locomotion of a crawling robot.

5. Case study: crawling robot

We designed a simple robot which uses origami towers as simple mechanisms which transform motor rotation to linear motion enabling a crawling gait, similar to an earthworm (see

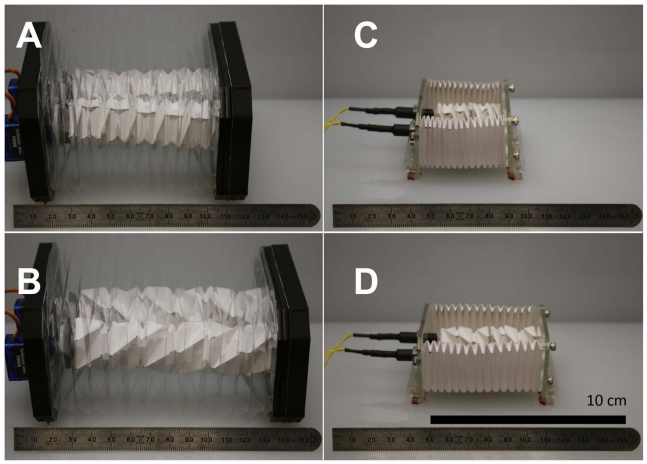

Figure 9. Photos of crawling robot showing scaling and actuation positions. (A) and (B) show large version in contracted and expanded positions respectively. Transparent PET is used for the bellow structure to show internal origami tower. Robot scaling can be accomplished by simply changing the scale of the CP. (C) and (D) show small crawling robot in contracted and expanded positions respectively.

figures 8 and 9). Our origami robot design is capable of crawling forward, and turning left and right due to the repeated expansion/contraction of two internal origami towers which can be actuated independently. Each origami tower is constructed from the CP shown in figure 12(A). Here, $n = 5$ and $\lambda = 6$ for each building block, and a tower of 6 building blocks is created by folding 6 connected rows of the pattern shown in figure 1(A). These towers are supported by a folded bellows structure which protects the origami towers, and allows free rotation of moving components. This folded bellow is attached to 3D printed faceplates which hold the motors and feet. Origami towers are connected to the faceplates with a friction disk which protects the structure from over rotation (rotation beyond the point where the tower is fully open or closed) which would damage the paper origami tower. Initially, the friction disk holds the front polygonal face of the origami tower fixed so that the motor can rotate the base of the tower to open or close the structure—motor angle therefore gives the rotation angle, α, measured with respect to the open configuration. When the tower is fully open or fully closed, the friction disk will slip with continued motor rotation, which prevents the motor from tearing the thin folded structure. The motors are driven in one direction to expand the tower and the opposite direction to contract it (the direction of rotation resulting in expansion is determined by the chirality of the tower). To prevent twisting of the structure and enforce straight motion, the two internal origami towers are designed to have opposite chirality as shown in figure 9. Forward net locomotion is obtained during each expansion-contraction cycle through anisotropic friction between the feet and the ground surface which allows forward motion but prevents back-slide.

Anisotropic friction is used by earthworms and snakes for locomotion and has been adopted in other origami inspired robots with similar gaits [9]. To realize this effect,

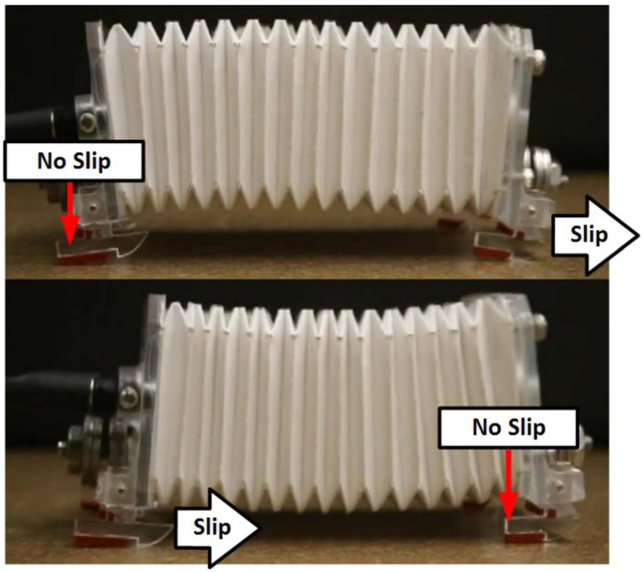

Figure 10. Still photos of foot showing anisotropic friction. Switching between surfaces occurs due to intrinsic torque which causes a rotation about the point of contact. The rounded smooth surface on the front allows the foot to slide forward, but the rubber protrusion in the rear of the foot prevents backslide. The extended section acts as a lever increasing the normal force on the high friction surface.

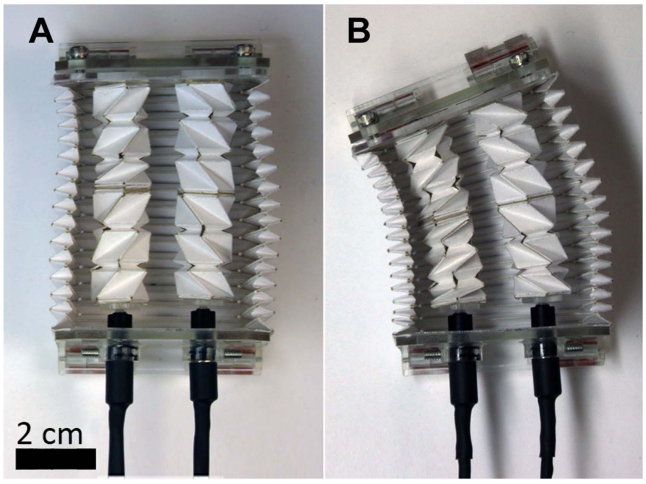

Figure 11. (A) Top view showing placement of origami towers with opposite chirality in straight orientation. Top of paper bellow removed for visibility. (B) Top view of turning motion. Left tower is contracting, right tower is expanded. Note that the front right rocking feet have flipped so that friction maintains this positon. While turning, faceplates are not parallel.

each foot has two surfaces with different frictional coefficients. The feet are attached to the faceplate so that they may rock back and forth so that either one of two surfaces is in contact with the ground due to the intrinsic reaction torque at the point of contact (figure 10). The front surface is smooth and rounded plastic with a low coefficient of friction (acrylic or Somos® WaterClear), while the back surface is a soft 10A durometer rubber with a high coefficient of friction. When the robot moves, the feet tilt forward between these faces so that the plastic surface facilitates forward sliding and the rubber surface prevents backslide as shown in figure 10.

The crawling gait cycle functions as follows (figure 9). Motor rotation causes expansion of the internal towers which opens the origami bellow body and slides the front feet forward. The friction pads on the rear feet (nearest to the motors) prevent backslide of the robot forcing it to expand in the forward direction. The internal tower structures are then contracted by turning the motors in the opposite direction. This contraction causes the entire robot to shrink in length causing the rear feet to rock onto the plastic surface then slide forward to meet the front feet. In this stage of motion, the friction pads on the front feet rock backward to engage with the ground to prevent backslide of the front face of the robot.

Left and right turning are facilitated using two independently driven origami towers mounted at the same height and symmetric about the midplane of the robot (figure 11(A)). By contracting the left tower and repeatedly expanding and contracting the right tower, the robot is made to turn left as shown in figure 11(B) and vice versa to turn right. During this turning motion, the robot structure assumes the arc shape shown in figure 11(B). While in this shape, the front and back bellow faces are no longer parallel. Since the origami towers are attached to the faceplates, and the origami structure kinematically maintains a parallel relationship between its polygonal faces during expansion and contraction, additional bending freedom must be added to the origami tower pattern to allow it to span and actuate the bellow structure while turning. This bending freedom was added in the form of a modification to the CP which is shown in figure 12(A) as compared to figure 1(A). The addition of panels and cuts between the rows/unit cells allow the towers to bend while maintaining a parallel relationship between polygonal faces of each unit cell. Additional folds provide bending freedom while cuts are made to minimize paper layers in flat folded state. Note that the analysis done in the previous sections applies to a single building block of the origami tower. This modification acts as a spherical hinge between the origami structures previously defined, and is therefore not included in the discussion of the structures themselves. The resulting folded tower, including modifications, is shown in figure 12(B) as a CAD model and paper versions in figure 12(C) at different scales which are produced by simply scaling the CP before folding. Arduino Uno is used to control the motors for 'forward', 'left' and 'right' locomotion. The specifications of the small and large robots are listed in table 1.

A power balance model can provide insights to relate the electrical properties of the motors to the mechanical properties of the external and internal origami structure. The input electrical power (P_{in}) is related to the mechanical output power (P_{out}) by the mechanical efficiency η:

$$\eta P_{\text{in}} = P_{\text{out}}, \tag{21}$$

$$P_{\text{in}} = T_{\text{motor}}\omega_{\text{motor}}. \tag{22}$$

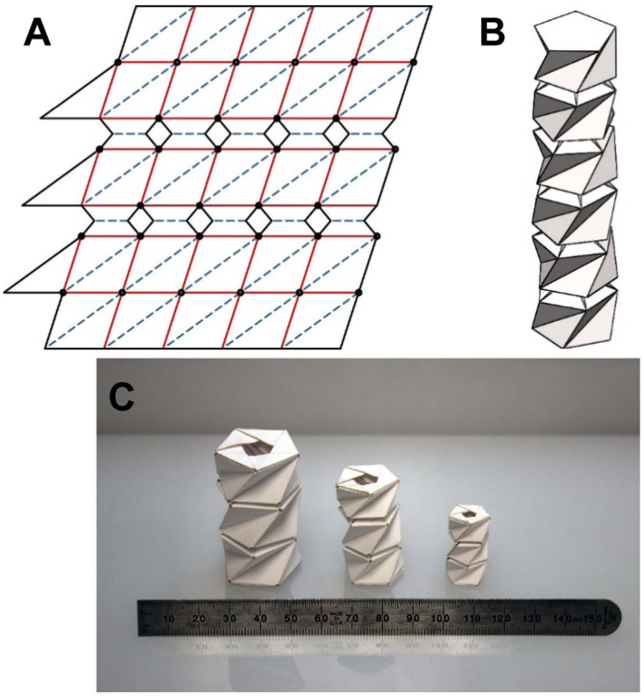

Figure 12. (A) Modified CP to provide bending freedom to internal origami tower. Blue dashed lines are valley folds. Red solid lines are mountain folds. Black lines and dots are through-cuts. Small cutout circles at vertices prevent tearing of paper. Tabs are for gluing and additional rows at the top and bottom are folded flat to provide a polygonal face (B) CAD model of flexible origami tower. (C) Photos of paper towers created from (A). Different sizes are shown to demonstrate scalability of origami folded mechanisms.

The motors' rotational speed and torque are defined as:

$$T_{\text{motor}} = -\frac{T_{\text{stall}}}{\omega_{\text{max}}}\omega_{\text{motor}} + T_{\text{stall}} \tag{23}$$

T_{stall} and ω_{max} are the stall toque and maximum rotational speed. Both of which are determined from the factory specifications of a given motor listed in table 1. The output mechanical power, P_{out}, is the average energy expended per unit locomotion time:

$$P_{\text{out}} = \frac{\sum E_{\text{tot}}}{\Delta t} \tag{24}$$

$$\sum E_{\text{tot}} = \frac{1}{2}mv^2 + \frac{1}{2}k_{\text{bellow}}\Delta l^2 + W_{\text{tower}} + W_{\text{friction}} \tag{25}$$

where v is the robot average velocity, m its mass, k_{bellow} its linear stiffness of the bellow and Δl its expansion (forward stroke). The energy expression is the respective summation of the robot's kinetic energy (first term), the potential energy stored in the external bellow (second term), the work done to expand/contract the internal origami tower (third term), and the friction dissipation work between the robot and the ground (last term). W_{tower} can be directly related to the strain energy of the internal bi-stable origami structure and its expression is shown in equation (16). The power balance model will be used to perform robot locomotion efficiency studies and take advantage of the bi-stable behavior of the origami structure to reduce the overall power consumption for a given mechanical efficiency.

Table 1. List of characteristic measurements of the robots shown in figure 9. L_f length measured foot to foot.

	Small	Large
Mass (g)	30.46	136.04
Robot Length (mm)	85	150
Max Forward Stroke (mm)	13	29
Forward Velocity (mm s^{-1})	2.1	11.8
Motor Type	DC Planetary Gearmotor	Servo FS90R

6. Summary

This work represents, to our knowledge, the first implementation of the concept of virtual folds to analyze panel bending in snapping Kresling-like origami towers. We demonstrate how this simple numerical scheme can be derived to solve both the kinematics and the forces without the need of computationally expensive finite element methods. Moreover, we show a new concept for linear actuation by nesting the Kresling-like tower to achieve linear motion from a motor fixed at the base. In addition to its use in robotics, this concept can have applications in the design of deployable booms. This manuscript presented the design and analysis of a bi-stable origami structure and its use in actuating a crawling robot gait. The crawling robot utilizes some of the advantages of the bistability such as being stable at any configuration, open, closed or bent during turning. This has advantages in the power consumption and makes the open loop locomotion control straight forward. However, there exists additional opportunities to leverage the multi-stability. This is the focus of future work and will be achieved in two stages: (a) we will tune our current open loop controller such that the motor rotates in multiples of the critical angle, where this multiple is the number of bi-stable building blocks, and (b) we will implement a control feedback loop. Both these changes will improve the power efficiency through exploiting the bistability of each of the building blocks.

Acknowledgments

The authors acknowledge support from the Mechanical Science and Engineering at the University of Illinois Urbana-Champaign through start-up funding.

ORCID iDs

S Tawfick https://orcid.org/0000-0003-3645-527X

References

[1] Forterre Y, Skotheim J M, Dumais J and Mahadevan L 2005 How the Venus flytrap snaps *Nature* **433** 421–6

[2] Son K, Guasto J S and Stocker R 2013 Bacteria can exploit a flagellar buckling instability to change direction *Nat. Phys.* **9** 494–8

[3] Smith M L, Yanega G M and Ruina A 2011 Elastic instability model of rapid beak closure in hummingbirds *J. Theor. Biol.* **282** 41–51

[4] Skotheim J M and Mahadevan L 2005 Physical limits and design principles for plant and fungal movement *Science* **308** 1308–10

[5] Mahadevan L and Rica S 2005 Self-organized origami *Science* **307** 1740 2008

[6] Kresling B 2012 Origami-structures in nature: lessons in designing 'smart' materials *Mater. Res. Soc. Symp. Proc.* **1420** 25–31

[7] Silverberg J L *et al* 2014 Applied origami. Using origami design principles to fold reprogrammable mechanical metamaterials *Science* **345** 647–50

[8] Silverberg J L *et al* 2015 Origami structures with a critical transition to bistability arising from hidden degrees of freedom *Nat. Mater.* **14** 389–93

[9] Onal C D, Wood R J and Rus D 2013 An origami-inspired approach to worm robots *IEEE/ASME Trans. Mechatronics* **18** 430–8

[10] Felton S, Tolley M, Demaine E, Rus D and Wood R 2014 A method for building self-folding machines *Science* **345** 644–6

[11] Miyashita S, Guitron S, Ludersdorfer M, Sung C R and Rus D 2015 An untethered miniature origami robot that self-folds, walks, swims, and degrades *2015 IEEE Int. Conf. on Robotics Automation (ICRA)* pp 1490–6

[12] Zhakypov Z, Falahi M, Shah M and Paik J 2015 The design and control of the multi-modal locomotion origami robot, Tribot *2015 IEEE/RSJ Int. Conf. on Intelligent Robots and Systems (IROS)* 4349–55

[13] Wilson L, Pellegrino S and Danner R 2013 Origami sunshield concepts for space telescopes *54th AIAA/ASME/ASCE/AHS/ASC Structures, Structural Dynamics, and Materials Conf.* pp 1–8

[14] Cai J, Ma R, Feng J, Zhou Y and Deng X 2016 Foldability analysis of cylindrical origami structures *Mech. Mach. Theory* **36** 1689–99

[15] Jianguo C, Xiaowei D, Yuting Z, Jian F and Ya Z 2016 Folding behavior of a foldable prismatic mast with Kresling origami pattern *J. Mech. Robot.* **8** 31004

[16] Nayakanti N, Tawfick S and Hart A J 2017 Twist-coupled kirigami metamaterials and mechanisms in preparation

[17] Cai J, Ma R, Feng J, Zhou Y and Deng X 2016 Foldability analysis of cylindrical origami structures *Mech. Mach. Sci.* **36** 143–51

[18] Schenk M and Guest S D 2013 Geometry of Miura-folded metamaterials *Proc. Natl Acad. Sci.* **110** 3276–81